General Two-Stage Model-Based Three-Component Hybrid Compact Polarimetric SAR Decomposition Method

Wentao Hou, Fengjun Zhao, Xiuqing Liu, and Robert Wang, *Senior Member, IEEE*

***Abstract*—Polarimetric decomposition is an effective way for synthetic aperture radar (SAR) data interpretation. As for hybrid compact polarimetric (HCP) SAR, there are mainly two different types of decomposition methods, including wave-dichotomy-theorem-based and model-based. However, the existing methods are not universal because they cannot estimate volume scattering component accurately in different scenes. In order to solve this problem, a general two-stage model-based three-component HCP decomposition method (GTM) is proposed by involving Arii volume scattering model. In the first stage, a method is designed to identify the dominant scattering mechanism (surface, dihedral, and volume scattering mechanism) of each pixel according to the characteristics of the three scattering models. Then, the GTM method is solved when the three basic scattering mechanisms are dominant, respectively, in the second stage. Two simulated HCP datasets are used to verify the performance of the decomposition method. The results show that GTM can more accurately identify the dominant scattering mechanism in different regions than existing methods, and it can obtain closer results to the quad-polarimetric method.**

***Index Terms*—Arii volume model, hybrid compact polarimetry, model-based, polarimetric decomposition.**

I. Introduction

COMPACT polarimetric synthetic aperture radar (SAR) is a special dual-polarimetric system and has advantages of simple system design, halved transmission power, and wider swath compared with a quad-polarimetric SAR. It can obtain more scattering information than a traditional linear dual-polarimetric SAR and sometimes achieve similar performance with quad-polarimetric SAR in many applications [1]. There are currently three different completely polarized (CP) modes, which are as follows.

Manuscript received November 21, 2020; revised February 5, 2021 and March 1, 2021; accepted March 3, 2021. Date of publication March 11, 2021; date of current version May 20, 2021. This work was supported in part by the National Key Research and Development Program of China under Grant 2017YFB0502700 and in part by the Beijing Municipal Natural Science Foundation under Grant 4192065. *(Corresponding author: Robert Wang.)*

Wentao Hou is with the Department of Space Microwave Remote Sensing System, Aerospace Information Research Institute, Chinese Academy of Sciences, Beijing 100094, China, and also with the School of Electronic, Electrical and Communication Engineering, University of Chinese Academy of Sciences, Beijing 100039, China (e-mail: houwentao17@mails.ucas.edu.cn).

Fengjun Zhao, Xiuqing Liu, and Robert Wang are with the Department of Space Microwave Remote Sensing System, Aerospace Information Research Institute, Chinese Academy of Sciences, Beijing 100094, China (e-mail: fjzhao@mail.ie.ac.cn; lucia@mail.ie.ac.cn; yuwang@mail.ie.ac.cn).

Digital Object Identifier 10.1109/JSTARS.2021.3065431

1) $\pi/4$ mode. Transmitting 45° linearly polarized waves and receiving H and V linearly polarized waves.
2) Dual circular polarimetric mode. Transmitting left- or right-handed circularly polarized waves and receives left- and right-handed circularly polarized waves.
3) Hybrid compact polarimetric (HCP) mode. Transmitting left- or right-handed circularly polarized waves and receiving H and V linearly polarized waves.

   Among them, HCP mode is the only one that has been applied to actual spaceborne systems for its unique performance, and many related research works are based on HCP mode [2].

Polarimetric target decomposition can effectively extract the features of ground objects. Some of the new research trends include polarimetric SAR image factorization [3], [4], scattering power decomposition [5], polarimetric-anisotropic decomposition [6], etc. The scattering power decomposition method mainly decomposes the target into various components, such as surface, dihedral, and volume scattering components. As for HCP data, there are primarily two different scattering power decomposition methods, wave-dichotomy-theorem-based (WDT-based) [7] and model-based decomposition methods.

The basic idea of WDT-based decomposition method is to decompose the received Stokes wave vector into the sum of two independent wave components, a CP wave, and a completely depolarized (CD) wave. Then, regards the CD wave as the volume scattering component, and further decomposes the CP wave into surface scattering and dihedral angle scattering components. The WDT-based method is simple and easy for implementation, but there are often over estimation for the volume scattering in urban areas [8]. $m-\delta$ method is one of the first proposed decomposition methods for compact polarimetry [9], [10]. Cloude *et al.* and Raney *et al.*, respectively, proposed the famous $m-\alpha$ [11] and $m-\chi$ [12] decomposition methods, which have been extensively used in classification [13] and crop monitoring [14]. Recently, Dey *et al.* use a parameter θ to characterize the scattering mechanism and proposed the $m-\theta$ method [5]. Bhattacharya *et al.* consider both the transmitted and received wave ellipticities and the orientation angles to calculate polarized power faction Ω and proposed $S-\Omega$ method [15]. Kumar *et al.* improved the $S-\Omega$ method based on the CPR to enhance the performance when surface scattering and dihedral scattering are dominant [16].

A model-based decomposition method has been widely used in quad-polarimetric SAR for its explicit physical significance [17], [18]. Guo *et al.* [19] first introduce Freeman decomposition into compact polarimetric data and Kumar *et al.* [8] further extended the method by introducing Yamaguchi volume model. However, these two methods are similar to DWT-based methods. First, the contribution of volume scattering component is estimated and separated to obtain a CP wave. Then, the CP wave is used to decomposed into surface scattering and dihedral scattering mechanisms. In addition, Wang *et al.* introduced a scale factor in volume component estimation [20]. It performs well in urban area, but it cannot represent the scattering characteristics of forest areas correctly.

In order to solve these problems, a general two-stage model-based HCP decomposition method (GTM) is proposed. Arii general volume scattering model [21], [22] is converted to the form of Stokes vector to enhance the characterization ability of volume scattering mechanism in compact polarimetry. In the first stage, an algorithm for distinguishing dominant scattering mechanisms is first designed depending on the characteristics of the three typical scattering mechanism models. In the second stage, considering the finite observation of compact polarimetry, the decomposition method is solved, respectively, under the condition that each scattering mechanism is dominant. The comparison with existing methods verifies the effectiveness of the GTM method, which has the optimal comprehensive performance when dealing with many different types of ground object scenes.

The rest of this article is structured as follows. Existing decomposition methods are first introduced in Section II. The methodology and solution of the proposed GTM method are then carried out in Section III. Section IV presents the results and discussion of the proposed and comparison methods. Theoretical performance and the effect of transmitting distortion analysis are given in Section V, and Section VI concludes this article.

II. HCP Data and Existing Works

A. HCP Data Description

HCP data can be emulated from quad-polarimetric SAR data. Considering the right-handed circularly polarized electromagnetic wave emission, the relationship between the HCP received Stokes vector and the quad-polarimetric coherency matrix is as follows [11]:

$$\mathbf{G} = \begin{bmatrix} g_0 \\ g_1 \\ g_2 \\ g_3 \end{bmatrix} = \frac{1}{2} \begin{bmatrix} (t_{11} + t_{22} + t_{33}) - 2\mathrm{Im}(t_{23}) \\ 2\mathrm{Re}(t_{12}) - 2\mathrm{Im}(t_{13}) \\ 2\mathrm{Im}(t_{12}) + 2\mathrm{Re}(t_{13}) \\ -(t_{22} + t_{33} - t_{11}) + 2\mathrm{Im}(t_{23}) \end{bmatrix} \tag{1}$$

where t_{ij} is the ith row jth column element in coherency matrix. $\mathrm{Re}(\cdot)$ and $\mathrm{Im}(\cdot)$ denote the real and imaginary part of $(\cdot)$, respectively.

B. Existing Decomposition Methods

1) WDT-Based Decomposition Methods: Any Stokes vector can be decomposed into a CP wave and a CD wave according to WDT

$$\mathbf{G} = \begin{bmatrix} g_0 \\ g_1 \\ g_2 \\ g_3 \end{bmatrix} = \mathbf{G}_{\mathrm{CP}} + \mathbf{G}_{\mathrm{CD}} = \begin{bmatrix} mg_0 \\ g_1 \\ g_2 \\ g_3 \end{bmatrix} + (1-m)g_0 \begin{bmatrix} 1 \\ 0 \\ 0 \\ 0 \end{bmatrix} \tag{2}$$

where $m = \sqrt{g_1^2 + g_2^2 + g_3^2}/g_0$ is the degree of polarization (DoP) of the wave $\mathbf{G}$. For CP wave, $m = 1$, whereas for CD wave, $m = 0$. As for WDT-based decomposition methods, the CD component is regarded as volume scattering, thus

$$P_v = (1-m)g_0. \tag{3}$$

Then, the CP component is split into surface and dihedral scattering components. Different methods have different decompose criterion. As for $m - \delta$ decomposition method [10], relative phase between H and V channel is adopted

$$\begin{cases} P_s = \frac{1}{2} m g_0 (1 + \sin\delta) \\ P_d = \frac{1}{2} m g_0 (1 - \sin\delta) \end{cases} \tag{4}$$

with $\delta = \tan^{-1}(g_3/g_2)$. As for $m - \chi$ decomposition method [12], ellipticity angle χ is used for distinguishing the two scattering mechanism

$$\begin{cases} P_s = \frac{1}{2} m g_0 (1 + \sin 2\chi) \\ P_d = \frac{1}{2} m g_0 (1 - \sin 2\chi) \end{cases} \tag{5}$$

with $\sin 2\chi = g_3/mg_0$. As reported, the result of $m - \alpha$ method is the same as $m - \chi$ decomposition method [23], thus, it will not be introduced separately in this article.

The basic idea of WDT-based decomposition methods is clear. However, it divides the scattering power into the surface and dihedral component based on a simple factor related to a certain polarimetric feature rather than based on a specific Stokes vector form. Therefore, we cannot obtain the specific component forms of the surface and the dihedral scattering component.

2) Model-Based Decomposition Methods: Wang *et al.* applied Freeman decomposition in quad-polarimetric to HCP decomposition [20]. Because of the characteristics of compact polarimetric, it is impossible to estimate the volume scattering component directly according to the t_{33} term as in quad-polarimetric. Wang *et al.* used the method of estimating the volume scattering component in WDT-based methods, and added a scale factor (in their experiments, they set $p = 0.65$)

$$P_v = p \cdot g_0 (1 - m). \tag{6}$$

This operation can reduce the overestimation of the volume scattering, but it also introduces a huge problem, in which the volume scattering component is always less than the total power. Thus, even the CD wave cannot be decomposed correctly. Kumar *et al.* [23] introduced Yamaguchi volume scattering model and proposed the HTM method. The Stokes vector is first decomposed into a volume scattering component and a joint component, which represents the contribution of surface scattering and dihedral scattering components. Then, the joint contribution was further decomposed into two basic scattering

mechanisms. However, as the joint contribution is a CP wave in the form, there is always one component whose power is 0 obtained by joint component decomposition. Therefore, each pixel is only decomposed into two components in this method.

III. Model Selection and GTM Algorithm

Due to the limited observation data of the compact polarimetric system, the following principles should be considered in model selection and solving process.

1) The model should describe the distribution characteristics of ground features as fine as possible.
2) Considering the problem of solving the decomposition method, there should not be too many unknown parameters in the model.
3) When a certain scattering component is not dominant, its model can be simplified.

A. Model Selection

According to the principles mentioned earlier, the characteristics of each scattering component under compact polarimetric are described in detail below. Referring to the quad-polarimetric decomposition method, surface and dihedral scattering is modeled by Bragg and Fresnel model, and the Stokes vector form is derived as following.

As for surface scattering

$$\mathbf{T}_s = f_s \begin{bmatrix} 1 & \beta^* & 0 \\ \beta & |\beta|^2 & 0 \\ 0 & 0 & 0 \end{bmatrix} \Rightarrow \mathbf{G}_s = \begin{bmatrix} |\beta|^2 + 1 \\ 2\mathrm{Re}[\beta] \\ -2\mathrm{Im}[\beta] \\ 1 - |\beta|^2 \end{bmatrix} \tag{7}$$

where $1/2$ coefficient is ignored. It should be noted that the model is a CP wave regardless of the β value. Especially, when the $\beta = 0$, the model degenerates to ideal surface scattering $\mathbf{G}_s = [1\ 0\ 0\ 1]^T$.

As for dihedral scattering

$$\mathbf{T}_d = f_s \begin{bmatrix} |\alpha|^2 & \alpha & 0 \\ \alpha^* & 1 & 0 \\ 0 & 0 & 0 \end{bmatrix} \Rightarrow \mathbf{G}_d = \begin{bmatrix} |\alpha|^2 + 1 \\ 2\mathrm{Re}[\alpha] \\ 2\mathrm{Im}[\alpha] \\ |\alpha|^2 - 1 \end{bmatrix} \tag{8}$$

where $1/2$ coefficient is ignored. It should be noted that the model is also a CP wave regardless of the α value. Especially, when $\alpha = 0$, the model degenerates to ideal dihedral scattering $\mathbf{G}_d = [1\ 0\ 0\ -1]^T$.

In Freeman decomposition, vegetation canopy was modeled as a cloud of uniformly distributed thin dipoles [17], and the corresponding Stokes vector is equal to CD wave. Later, Yamaguchi *et al.* developed a new volume scattering model by changing the probability density function (pdf) of canopy distribution [18]. The volume scattering model derived from the fixed dipole distribution is not widely applicable, so some more universal volume scattering models have been proposed.

Freeman first assumed that the backscattering coefficient of vegetation canopy obeys the condition of azimuthal symmetry (usually observed in natural terrain) [24], and introduced a "shape parameter" ρ to make it more flexible to model the volume scattering. An *et al.* further extended the model and discussed its applicability [25]. However, this model assumed the echo between polarization channels is equal, which seriously limits its applicable scenarios. In order to address this problem, Antropov *et al.* further introduced the imbalance between copolarization channels to model the covariance matrix generally [26]. In addition, Neumann *et al.* [27] and Arii *et al.* [21], [22], respectively, established models for the distribution characteristics of the vegetation canopy and derived the corresponding universal volume scattering model.

Among all general volume scattering models, Arii volume scattering model follows the derivation method of the Freeman or Yamaguchi volume scattering model, which is often selected in quad-polarimetric decomposition method and has good performance. In addition, the Arii model has fewer model parameters than Neumann model, and it retains good performance after it is transformed into the Stokes vector form. Thus, we adopted this model in our proposed method. The derived coherency matrix of Arii volume scattering model is

$$\mathbf{T}_v(\theta_0, \sigma) = \mathbf{T}_\alpha + p(\sigma)\mathbf{T}_\beta(2\theta_0) + q(\sigma)\mathbf{T}_\gamma(4\theta_0) \tag{9}$$

where

$$\mathbf{T}_\alpha = \frac{1}{4}\begin{bmatrix} 2 & 0 & 0 \\ 0 & 1 & 0 \\ 0 & 0 & 1 \end{bmatrix} \tag{10}$$

$$\mathbf{T}_\beta(2\theta_0) = \frac{1}{4}\begin{bmatrix} 0 & -\cos(2\theta_0) & \sin(2\theta_0) \\ -\cos(2\theta_0) & 0 & 0 \\ \sin(2\theta_0) & 0 & 0 \end{bmatrix} \tag{11}$$

$$\mathbf{T}_\gamma(4\theta_0) = \frac{1}{4}\begin{bmatrix} 0 & 0 & 0 \\ 0 & \cos(4\theta_0) & -\sin(4\theta_0) \\ 0 & -\sin(4\theta_0) & -\cos(4\theta_0) \end{bmatrix} \tag{12}$$

$$p(\sigma) = 2.0806\sigma^6 - 6.3350\sigma^5 + 6.3864\sigma^4 - 0.4431\sigma^3 - 3.9638\sigma^2 - 0.0008\sigma + 2.000 \tag{13}$$

$$q(\sigma) = 9.0166\sigma^6 - 18.7790\sigma^5 + 4.9590\sigma^4 + 14.5629\sigma^3 - 10.8034\sigma^2 + 0.1902\sigma + 1.000. \tag{14}$$

In (9), θ_0 and σ represent the mean orientation angle and randomness, respectively. Higher σ indicating stronger randomness and more approximate to a uniform distribution. Converting Arii volume model into Stokes vector form using (1)

$$\mathbf{G}_v = \begin{bmatrix} 1 \\ -m_v \cos 2\theta_0 \\ m_v \sin 2\theta_0 \\ 0 \end{bmatrix} \tag{15}$$

where $1/2$ coefficient is ignored. $m_v = p(\sigma)/2$ is DoP of volume scattering model, which depends on the randomness and m_v decreases with the increase of randomness. When the randomness tends to infinity (canopy follows the uniform distribution), the model degenerates to the Freeman volume model, and the corresponding Stokes vector is in the form of CD wave.

According to the polarization theory, vegetation canopy shows a depolarization effect, so the value of m_v should be at a relatively low level. Arii has also verified in experiments [22] that for most vegetation coverage areas, the mean value of σ is greater than 0.66. Thus, the value of m_v has an upper limit. This point will be discussed further in Section III. In addition, it should be noted that the average orientation angle parameter θ_0 does not affect the DoP of the volume scattering model. Therefore, m_v only contains information related to canopy randomness.

B. Proposed GTM Decomposition Method

In order to reduce the number of unknowns, cases dominated by three scattering components are considered, respectively.

1) Surface Scattering Mechanism Dominant: When the surface scattering is dominant, Bragg surface scattering model, ideal dihedral scattering model, and Freeman volume scattering model are adopted for decomposition. Then, the decomposition method is expressed as

$$\begin{aligned}\mathbf{G} &= f_s\mathbf{G}_s + f_d\mathbf{G}_d + f_v\mathbf{G}_v \\ &= f_s\begin{bmatrix}|\beta|^2+1\\ 2\mathrm{Re}[\beta]\\ -2\mathrm{Im}[\beta]\\ 1-|\beta|^2\end{bmatrix} + f_d\begin{bmatrix}1\\0\\0\\-1\end{bmatrix} + f_v\begin{bmatrix}1\\0\\0\\0\end{bmatrix}.\end{aligned} \tag{16}$$

Expanding

$$\begin{cases} g_0 = f_s(|\beta|^2+1) + f_d + f_v \\ g_1 = 2f_s\mathrm{Re}[\beta] \\ g_2 = -2f_s\mathrm{Im}[\beta] \\ g_3 = f_s(1-|\beta|^2) - f_d \end{cases}. \tag{17}$$

Thus, we can get the solution

$$\begin{cases} P_s = f_s(|\beta|^2+1) = \frac{(|\beta|^2+1)}{2|\beta|}\sqrt{g_1^2+g_2^2} \\ P_d = f_d = -g_3 + \frac{1-|\beta|^2}{2|\beta|}\sqrt{g_1^2+g_2^2} \\ P_v = f_v = g_0 + g_3 - \frac{1}{|\beta|}\sqrt{g_1^2+g_2^2} \end{cases} \tag{18}$$

where the phase of β is equivalent to the phase of $g_1 - jg_2$. If $|\beta|$ value can be estimated, then the problem can be solved properly. Considering the physical meaning, scattering power of each component should be nonnegative. It is easy to prove that $P_s \geq 0$, then

$$\begin{cases} P_d \geq 0 \\ P_v \geq 0 \end{cases} \Rightarrow \begin{cases} |\beta| \geq \frac{\sqrt{g_1^2+g_2^2}}{g_0-g_3} \\ |\beta|^2 + \frac{2g_3}{\sqrt{g_1^2+g_2^2}}|\beta| - 1 \leq 0 \end{cases}. \tag{19}$$

Further solving the right terms in (19) using quadratic equation knowledge, we can obtain the feasible solution interval of $|\beta|$

$$|\beta| \in \left[\frac{\sqrt{g_1^2+g_2^2}}{g_0+g_3}, \frac{mg_0-g_3}{\sqrt{g_1^2+g_2^2}}\right]. \tag{20}$$

When $|\beta|$ takes the value of left endpoint, the estimation of volume scattering is 0. When $|\beta|$ takes the value of right endpoint, the estimation of dihedral scattering is 0. As the scattering mechanisms are complex in real images, it is not common for a single component to be 0. Here, we use the midpoint of the feasible solution interval as an estimator for $|\beta|$. Thus, the proposed decomposition method under the surface scattering mechanism dominant is solved properly. Furthermore, it is easy to verify that if and only if the echo is a CP wave, i.e., $m = 1$, the endpoints of the interval are equal. In this special case, the echo can be regarded as the form of Bragg model, thus the power should only assign to surface scattering mechanism, and our decomposition results is consistent with the analysis with $P_s = g_0, P_d = 0,$ and $P_v = 0$.

2) Dihedral Scattering Mechanism Dominant: When the dihedral scattering is dominant, the Fresnel scattering model, ideal surface scattering model, and Freeman volume scattering model are adopted for decomposition. Then, the decomposition method is expressed as

$$\begin{aligned}\mathbf{G} &= f_s\mathbf{G}_s + f_d\mathbf{G}_d + f_v\mathbf{G}_v \\ &= f_s\begin{bmatrix}1\\0\\0\\1\end{bmatrix} + f_d\begin{bmatrix}|\alpha|^2+1\\ 2\,\mathrm{Re}[\alpha]\\ 2\,\mathrm{Im}[\alpha]\\ |\alpha|^2-1\end{bmatrix} + f_v\begin{bmatrix}1\\0\\0\\0\end{bmatrix}.\end{aligned} \tag{21}$$

Expanding

$$\begin{cases} g_0 = f_s + f_d(|\alpha|^2+1) + f_v \\ g_1 = 2f_d\mathrm{Re}[\alpha] \\ g_2 = 2f_d\mathrm{Im}[\alpha] \\ g_3 = f_s + f_d(|\alpha|^2-1) \end{cases}. \tag{22}$$

Thus, we can get the solution

$$\begin{cases} P_s = f_s = g_3 + \frac{1-|\alpha|^2}{2|\alpha|}\sqrt{g_1^2+g_2^2} \\ P_d = f_d(|\alpha|^2+1) = \frac{|\alpha|^2+1}{2|\alpha|}\sqrt{g_1^2+g_2^2} \\ P_v = f_v = g_0 - g_3 - \frac{1}{|\alpha|}\sqrt{g_1^2+g_2^2} \end{cases} \tag{23}$$

where the phase of α is equivalent to the phase of $g_1 + jg_2$. Once the value $|\alpha|$ is determined, the problem can be solved properly. Referring to the derivation when surface scattering dominant, the feasible solution of $|\alpha|$ can be obtained considering the nonnegative constrains

$$|\alpha| \in \left[\frac{\sqrt{g_1^2+g_2^2}}{g_0-g_3}, \frac{mg_0+g_3}{\sqrt{g_1^2+g_2^2}}\right]. \tag{24}$$

When $|\alpha|$ takes the value of left endpoint, the estimation of volume scattering is 0. When $|\alpha|$ takes the value of right endpoint, the estimation of surface scattering is 0. Here, the midpoint of the feasible solution interval is also used as an estimator for $|\alpha|$. Thus, the proposed decomposition method under the surface scattering mechanism dominant is solved properly. Furthermore, if and only if $m = 1$, the endpoints of the interval are equal, then the echo can be regarded as the form of Fresnel model, thus the power should only assign to dihedral scattering mechanism, and our decomposition results are consistent with the analysis with $P_s = 0, P_d = g_0,$ and $P_v = 0$.

3) Volume Scattering Mechanism Dominant: When the volume scattering is dominant, the Arii volume scattering model,

ideal surface model, and dihedral model are adopted for decomposition. Then, the decomposition method is expressed as

$$\begin{aligned}\mathbf{G} &= f_s\mathbf{G}_s + f_d\mathbf{G}_d + f_v\mathbf{G}_v \\ &= f_s\begin{bmatrix}1\\0\\0\\1\end{bmatrix} + f_d\begin{bmatrix}1\\0\\0\\-1\end{bmatrix} + f_v\begin{bmatrix}1\\-m_v\cos 2\theta_0\\m_v\sin 2\theta_0\\0\end{bmatrix}.\end{aligned} \tag{25}$$

Expanding

$$\begin{cases} g_0 = f_s + f_d + f_v \\ g_1 = -f_v m_v \cos 2\theta_0 \\ g_2 = f_v m_v \sin 2\theta_0 \\ g_3 = f_s - f_d \end{cases}. \tag{26}$$

The solution can be obtained as

$$\begin{cases} P_s = f_s = \frac{g_0+g_3}{2} - \frac{1}{2m_v}\sqrt{g_1^2+g_2^2} \\ P_d = f_d = \frac{g_0-g_3}{2} - \frac{1}{2m_v}\sqrt{g_1^2+g_2^2} \\ P_v = f_v = \frac{1}{m_v}\sqrt{g_1^2+g_2^2} \end{cases} \tag{27}$$

where θ_0 can be solved by $\tan 2\theta_0 = -g_2/g_1$. Considering the nonnegative power constrains of surface and dihedral scattering, the feasible interval for m_v is

$$\begin{cases} f_s \geq 0 \\ f_d \geq 0 \end{cases} \Rightarrow m_v \geq \max\left\{\frac{\sqrt{g_1^2+g_2^2}}{g_0+g_3}, \frac{\sqrt{g_1^2+g_2^2}}{g_0-g_3}\right\}. \tag{28}$$

As the assumption that volume scattering mechanism dominant in this case, a reasonable way for estimating m_v is to maximum the volume scattering power in (26). Thus, under this condition, m_v equal to the left endpoint of the feasible interval.

C. Discrimination of Dominant Scattering Mechanism

The three main scattering mechanisms have been modeled properly earlier, and the decomposition methods have been designed, respectively, under the dominance of the three scattering mechanisms. The next main task is to determine the dominant scattering mechanism for each pixel. It can be seen from (7), (8), and (15) that g_3 is only affected by surface or dihedral scattering mechanism, and the surface scattering mechanism makes g_3 to be positive, whereas dihedral scattering mechanism makes g_3 to be negative. Therefore, the dominance of the two scattering mechanisms can be judged based on the sign of g_3, i.e., when $g_3 > 0$, it can be considered as the dominant surface scattering; when $g_3 \leq 0$, it is the dominant dihedral scattering. It is worth noting that the aforementioned conclusions are only applicable to the case of emitting right-handed circularly polarized electromagnetic wave. When emitted left-handed circularly electromagnetic wave, surface scattering and dihedral scattering make g_3 be negative and positive, respectively. These conclusions are consistent with the previous studies [20], [23].

Since the volume scattering mechanism does not contribute to g_3, it is necessary to remove the volume scattering dominant region before using g_3 to distinguish between surface and dihedral scattering mechanisms. As mentioned earlier, the volume scattering model describes the depolarization effect, so the value

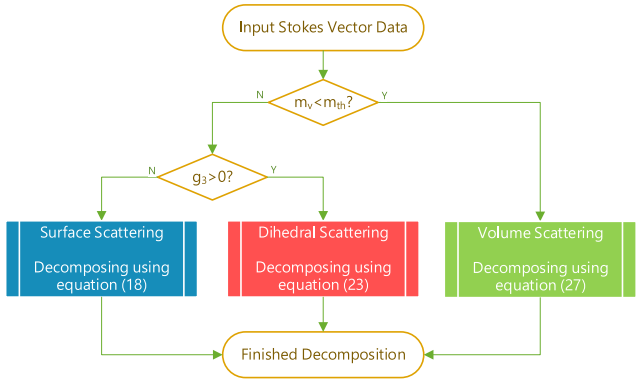

Fig. 1. Flowchart of proposed GTM method.

range of m_v is limited, reflecting the distribution characteristics of the vegetation canopy. Arii *et al.*'s inversion result [22] based on quad-polarimetric SAR data shows that the average value of σ in the forest area is greater than 0.66. Thus, the corresponding m_v in compact polarimetric data is less than 0.37. In the proposed method, if all pixels are assumed to be dominated by volume scattering mechanism, and m_v is estimated according to Section III, interesting conclusions will be drawn. For buildings and water areas, invalid estimates greater than one are often obtained due to the inadaptability of the model. However, the estimated m_v in the vegetation area is small, which characterizes the depolarization characteristic. Therefore, the vegetation area can be extracted by simple threshold segmentation based on these characteristics. In addition, as the size of the multilook window increases, m_v estimate of this proposed method is also decreased (randomness increased), which is similar to the quad-polarimetric result. Therefore, threshold mth can be set to distinguish the region where volume scattering is dominant.

In summary, the two-stage decomposition method has been constructed and the specific flowchart is illustrated in Fig. 1. In the first stage, the dominant scattering mechanism is determined, and in the second stage, the decomposition method is completed in three cases. In the next section, we will show the performance of the method on GF-3 and RADARSAT-2 emulated data.

IV. Results

A. Dominant Scattering Mechanism Identification

To evaluate the performance of the proposed method, a quad-polarimetric image of GF-3 satellite (acquired on March 27, 2019) in San Francisco, CA, USA is selected. The rows and columns of the image correspond to range direction and azimuth direction, respectively. This scenario includes urban areas with different orientation from the radar line of sight (LOS), forest, and water areas. The pixel distance of GF-3 is 2.48 m in range direction and 5.29 m in the azimuth direction. The window size was set as 7×3, corresponding to 15.7 by 15.9 m on the ground area. Besides, the nonlocal filter is utilized to reduce the impact of speckle noise. The details of the algorithm and the corresponding filter window size setting can refer to Chen *et al.* [28]. Fig. 2(a) shows the optical image of the area and five

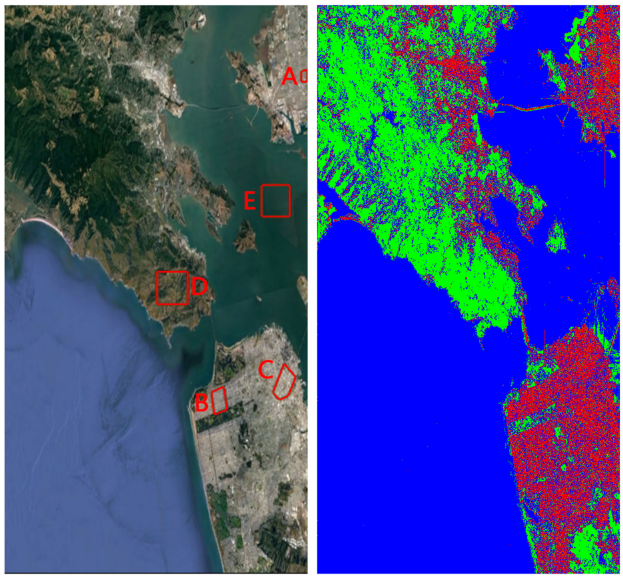

(a) (b)

Fig. 2. (a) Google Earth optical image of corresponding to the research area. (b) Distinguishing result of dominant scattering mechanism. Red, blue, and green pixels indicate that they are dominated by the dihedral, surface, or volume scattering mechanism, respectively.

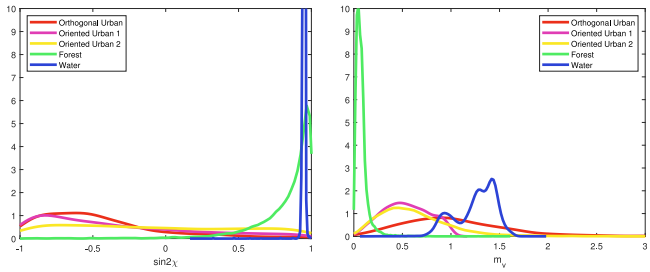

(a) (b)

Fig. 3. (a) PDF of $\sin 2\chi$ in five ROIs. (b) PDF of m_v in five ROIs.

ROIs are labeled by the red-colored boxes for further statistics analysis, namely A (Orthogonal Urban Area), B (Oriented Urban Area 1), C (Oriented Urban Area 2), D (Forest Area), and E (Water Area), respectively. Noticing the orientation angle of Patch C is higher than Patch B.

HCP data are emulated from quad-polarimetric data using (1). First, the characteristics of g_3 sign for different targets are analyzed. In order to display the distribution characteristics of g_3 sign under different echo intensities in one figure, we use the sine of the ellipticity angle $\sin 2\chi$ instead of g_3. It is obvious that $\sin 2\chi \in [-1, 1]$ and the sign of $\sin 2\chi$ is consistent with g_3. Therefore, analyzing the sign characteristics of $\sin 2\chi$ is equivalent to g_3. Fig. 3(a) displays the distribution of $\sin 2\chi$ for five ROIs.

From Fig. 3(a), the entire water area dominated by surface scattering is distributed on the positive axis. The orthogonal urban area dominated by dihedral scattering and Oriented Urban 1 is mainly distributed on the negative axis, and the proportions of negative elements are 85.54% and 74.91%, respectively. Therefore, the two main scattering mechanisms can be distinguished by the sign of g_3 element. It is worth noting that $\sin 2\chi$ in Oriented Urban 2 area has both positive and negative values. A possible reason is that the scattering mechanism becomes complicated as the orientation angle of the building increases. Thus, the dihedral scattering may no longer be dominant in Oriented Urban 2 area. In the forest area, $\sin 2\chi$ is mainly distributed near the positive axis. This indicates that in addition to the volume scattering mechanism in the forest area, there is also a surface scattering mechanism. These surface scattering mechanisms mainly come from the canopy or the ground and this phenomenon is consistent with the actual situation [29]. In particular, $\sin 2\chi = 0.75$ can better distinguish the surface or dihedral scattering dominant area in the GF-3 dataset. This is because the dominant area of surface scattering in this dataset is water, and its scattering mechanism is relatively pure, which results in a more concentrated distribution of $\sin 2\chi$. However, for areas where the scattering mechanism is not so pure, the adaptive threshold may also cause certain misjudgments. Therefore, in order to enable the method to have versatility for different ground objects, we still use $g_3 = 0$ as the threshold to distinguish the dominant area of surface and dihedral scattering mechanism.

Next, we will introduce the threshold selection for separating the volume scattering dominant area. For the five ROIs introduced earlier, m_v is calculated under the assumption that volume scattering is dominant, and Fig. 3(b) demonstrates its statistical pdf.

From Fig. 3(b), the estimated value of m_v forest area is smaller compared with other areas. This phenomenon shows a depolarization effect, which is consistent with the previous analysis. The estimated m_v of the orthogonal urban areas and water areas exhibiting standard dihedral scattering and surface scattering mechanisms is far from the theoretical range. This is caused by the mismatch between the model and the data, and we use this feature to distinguish different types of features. For oriented urban area, the probability density distribution moves to a smaller value relative to the overall orthogonal urban area. This is due to its rotation relative to the radar LOS, which leads to the introduction of volume scattering components. Therefore, according to the pdf of the forest and the oriented urban area, the threshold $m\text{th} = 0.2$ can be set to separate the forest area. According to the distinguishing rule of dominant scattering mechanism in Fig. 1, we can complete the classification of dominant scattering mechanism category. The result of the classification is shown in Fig 2(b). Red pixels indicate that they are dominated by the dihedral scattering mechanism, blue pixels indicate that they are dominated by the surface scattering mechanism, and green pixels indicate that they are dominated by the volume scattering mechanism. Compared with the optical image, it can conclude that the classification results of the dominant scattering mechanism are basically consistent with the types of ground objects.

B. Decomposition Results

Four existing methods are chosen for comparison, i.e., $m - \delta$ [10], $m - \chi$ [12], Wang *et al.*'s [20], and HTM [23] methods.

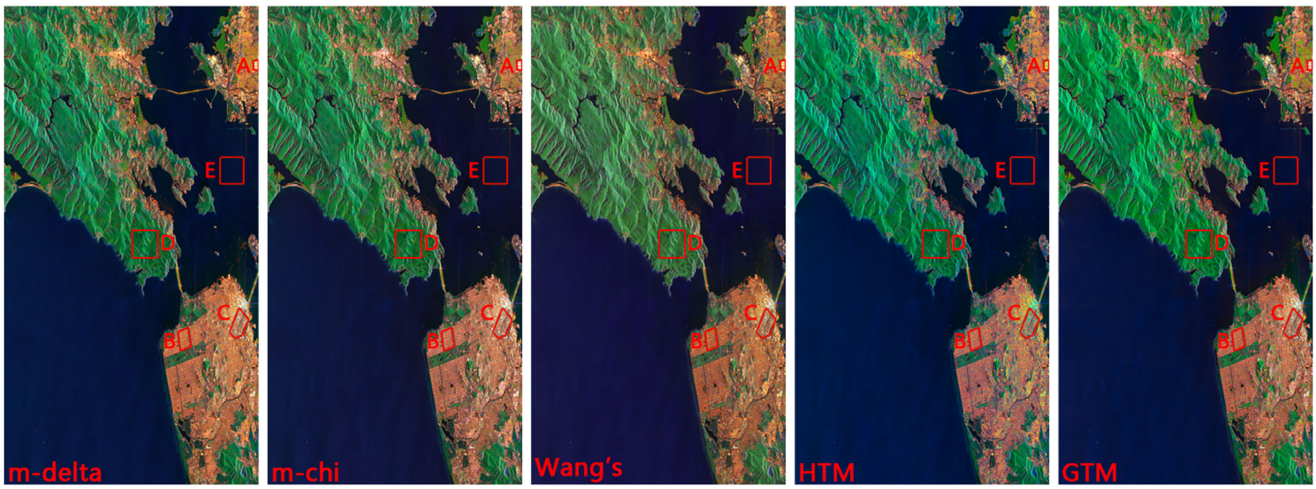

Fig. 4. Decomposition result of the emulated GF-3 HCP image. Red channel for dihedral scattering, green channel for volume scattering, and blue channel for surface scattering. (a) $m-\delta$ decomposition method. (b) $m-\chi$ decomposition method. (c) Wang's decomposition method. (d) HTM decomposition method. (e) GTM decomposition method.

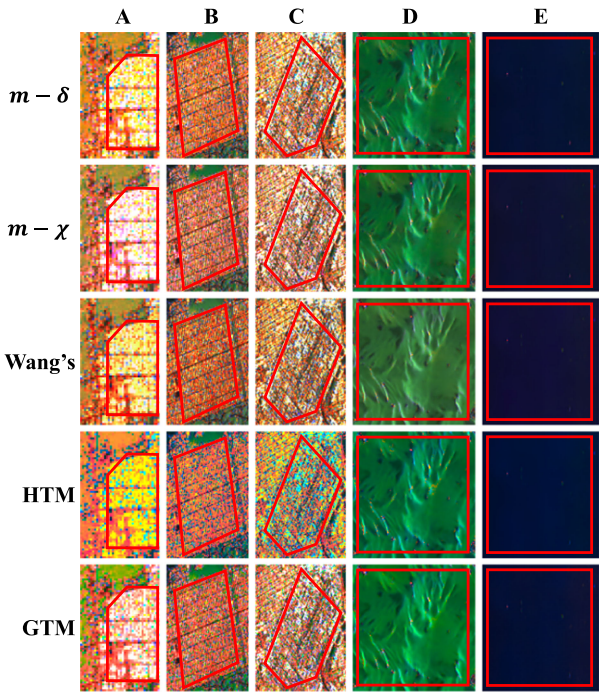

Fig. 5. Enlarged view of Patch A (Orthogonal Urban), Patch B (Oriented Urban 1), Patch C (Oriented Urban 2), Patch D (Forest), and Patch E (Water) in Fig. 4.

Fig. 4 shows the pseudocolor-coded images of five decomposition methods. The enlarge view of five ROIs is given in Fig. 5 and the corresponding detailed statistical information can be found in Table I.

The ability to highlight the dominant scattering mechanism in the target area is an important indicator for evaluating the pros and cons of a decomposition method [5]. Building in Patch A is orthogonal to the radar LOS and characterizes double-bounce scattering mechanism for the dihedral structure composed of building walls and ground surface. The statistical information in Table I indicates that all the decomposition methods can well determine that the dihedral scattering mechanism is predominant. Compared with the WDT-based method, the model-based decomposition method shows better performance in this region. Among them, the dihedral angle scattering component obtained by GTM method accounts for a relatively higher proportion of 83.22%, which is 6.45% and 16.64% higher than the two WDT-based methods, respectively. This phenomenon is related to the overestimation of volume scattering component in WDT-based method [8]. In addition, compared with the other two model-based decomposition methods, the proposed GTM method further reduces the volume scattering component by 1.00% and 4.11%, respectively.

For the forest area dominated by volume scattering mechanism, the contribution of the volume scattering component obtained by Wang's method is much lower than the other four decomposition methods. This is due to the fact that the volume scattering component of the region is greatly underestimated by using the scale factor. The other four methods have little difference in the estimation of volume scattering, which are 84.20%, 84.20%, 84.05%, and 84.87%, respectively, and GTM method is relatively higher. In addition to the volume scattering component, the surface scattering component is dominant. This is also consistent with the conclusion of analyzing the scattering characteristics of forest areas in Section IV-A. For the water area dominated by surface scattering, the model-based decomposition method also shows better performance and can get a relatively higher contribution of surface scattering components. The mean proportions of surface scattering power are 85.82%, 84.27%, and 86.84% for Wang's, HTM, and GTM, respectively. In this region, the proposed method also shows good performance. It can not only estimate higher surface scattering components, but also reduce the volume scattering contribution

TABLE I
STATISTICS OF GF-3 IMAGE DECOMPOSITION RESULTS

	Orthogonal Urban			Oriented Urban 1			Oriented Urban 2			Forest			Water		
	P_d	P_v	P_s	P_d	P_v	P_s	P_d	P_v	P_s	P_d	P_v	P_s	P_d	P_v	P_s
$m-\delta$	76.77	15.37	7.86	54.27	32.93	12.79	29.21	28.19	42.60	1.01	84.20	14.79	0.24	17.09	82.66
$m-\chi$	66.58	15.37	18.04	50.79	32.93	16.28	29.72	28.19	42.08	1.52	84.20	14.28	2.10	17.09	80.81
Wang's	82.84	9.99	7.17	63.40	21.41	15.20	36.06	18.33	45.61	15.78	54.73	29.49	3.07	11.11	85.82
HTM	82.48	13.10	4.42	60.78	29.53	9.69	32.48	25.54	41.98	0.56	84.05	15.39	0.00	15.73	84.27
GTM	83.22	8.99	7.79	63.35	21.31	15.34	36.12	18.22	45.66	1.06	84.87	14.07	4.14	9.01	86.84

Note: Scattering mechanisms contribution (%) of different decomposition methods in five ROIs.

TABLE II
GF-3 QUAD-POLARIMETRIC DECOMPOSITION RESULT USING G4U METHOD

	P_d	P_v	P_s	P_c
Orthogonal Urban	86.78	0.61	12.52	0.09
Oriented Urban 1	63.46	9.23	24.09	3.22
Oriented Urban 2	31.63	14.91	49.06	4.40
Forest	3.54	75.92	19.07	1.47
Water	4.46	9.07	86.30	0.17

Note: Statistical analysis of the scattering mechanisms contribution (%) in five ROIs.

by 8.08%, 2.10%, and 6.72% compared with $m-\chi$, Wang's, and HTM methods.

Since the scattering mechanism is more complicated for two oriented urban areas, we introduce the decomposition results of the quad-polarimetric SAR data as a reference. Considering the complexity of the scene, we choose the general four-component decomposition method (G4U) for comparison [30]. Table II lists the contribution of the scattering mechanism in the five ROIs under G4U method.

From the decomposition results of G4U, the dihedral scattering mechanism is still the main scattering mechanism in Oriented Urban Area 1, and the contribution of dihedral scattering reaches 63.46%. As for HCP decomposition method, the contributions of the average power of the dihedral scattering component in $m-\delta, m-\chi$, Wang's, HTM, and GTM are about 54.27%, 50.79%, 63.40%, 60.78%, and 63.35%, respectively. It is obvious that the model-based decomposition methods can obtain a result closer to G4U. The dihedral scattering component in $m-\chi$ method is the smallest, but it still shows its dominance. Except for the dihedral scattering component, the proportion of the surface scattering component in quad-polarimetric result is larger than the volume scattering component. In the HCP decomposition results, without exception, the proportion of volume scattering is higher. However, a trend can also be inferred from the results, the model-based method can obtain a lower contribution of the volume scattering component than the WDT-based decomposition method. In addition, the proposed GTM method also further reduces the contribution of volume scattering components, which are 11.62%, 0.1%, and 8.22% compared with $m-\chi$, Wang's, and HTM, respectively.

In Oriented Urban 2 with larger orientation angle, the quad-polarimetric decomposition results show that this area has both strong surface and dihedral scattering components, and the surface scattering components are relatively high. A possible reason is that the original quasi "wall-ground" dihedrallike structure becomes the quasi "wall-wall-ground" trihedrallike structure with the increasing of orientation angle. Thus, the contribution of surface scattering increased. The results of the five HCP decomposition methods also showed a consistent trend with the quad-polarimetric results. The contributions of the average power of the surface scattering component are 42.60%, 42.08%, 45.61%, 41.98%, and 45.66% and the contributions of the average power of the dihedral scattering component obtained by the five decomposition methods are 29.21%, 29.72%, 36.06%, 32.48%, and 36.12%, respectively.

As the volume scattering component estimated by the Wang's method is 0.65 times that the WDT-based decomposition method, its volume scattering component is also relatively low. Therefore, in areas, such as cities and water areas where volume scattering is not dominant, Wang's method can achieve similar results to the proposed method. However, its results in the forest area are almost unusable because of the underestimation of the volume scattering component. The proposed method overcomes its shortcomings and performs well in all different areas.

Next, we further quantitatively evaluate the similarity between HCP and quad-polarimetric decomposition results. Although the decomposition result of G4U has one more helix component than HCP, the contribution of this component is very small, which does not exceed 5% at most. Therefore, we ignore this component and compare the similarity of the results of the other three components. Decomposition vector $\vec{P}^{\mathrm{X}} = [\, P_d^{\mathrm{X}} \;\; P_v^{\mathrm{X}} \;\; P_s^{\mathrm{X}} \,]$ is defined to represent the decomposition result of quad-polarimetric and HCP, where X represents QP or HCP. For example, the decomposition vector of orthogonal urban area is $\vec{P}^{\mathrm{HCP}} = [\, 0.7677 \;\; 0.1537 \;\; 0.0786 \,]$ for $m-\delta$ method. The cosine angle is used to compare the similarity between different decomposition vectors and the definition is presented as

$$\phi = \cos^{-1} \frac{\vec{P}^{\mathrm{QP}} \cdot \vec{P}^{\mathrm{HCP}}}{|\vec{P}^{\mathrm{QP}}| \cdot |\vec{P}^{\mathrm{HCP}}|}. \tag{29}$$

Since $\vec{P}^{\mathrm{X}}$ is a nonnegative vector, it easy to conclude $\phi \in [0^\circ, 90^\circ]$. Smaller ϕ indicates that the two vectors are more similar, and the corresponding HCP decomposition result is closer to the quad-polarimetric decomposition result.

Considering the helix component is ignored in quad-polarimetric decomposition vector, the sum of the three elements in $\vec{P}^{\mathrm{QP}}$ will be less than one. However, (29) shows that the cosine angle has no relationship with the modulus of the decomposition

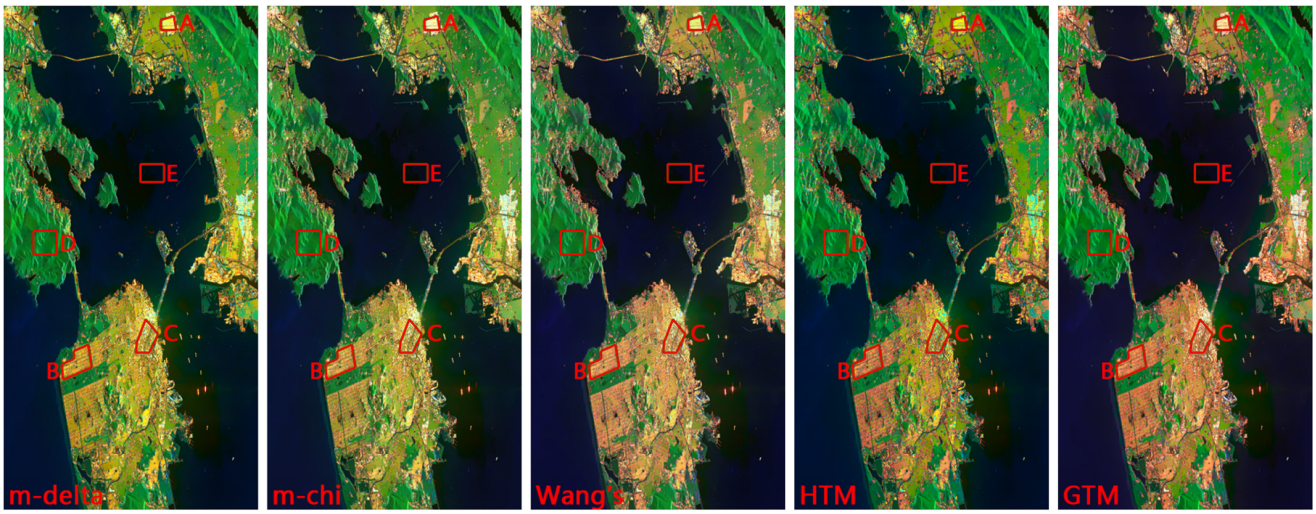

(a) (b) (c) (d) (e)

Fig. 6. Decomposition result of the emulated RADARSAT-2 HCP image. (a) $m-\delta$ decomposition method. (b) $m-\chi$ decomposition method. (c) Wang's decomposition method. (d) HTM decomposition method. (e) GTM decomposition method.

TABLE III
COSINE ANGLE (°) BETWEEN THE HCP AND QUAD-POLARIMETRIC DECOMPOSITION RESULTS (G4U) OF GF-3 DATA

	$m-\delta$	$m-\chi$	Wang's	HTM	GTM
Orthogonal Urban	11.12	13.98	7.23	10.02	**6.41**
Oriented Urban 1	23.89	24.11	12.63	21.09	**12.49**
Oriented Urban 2	14.37	14.53	6.18	12.27	**6.14**
Forest	4.56	4.74	18.24	**4.33**	5.05
Water	6.32	6.12	1.65	5.44	**0.24**
AVERAGE	12.05	12.70	9.19	10.63	**6.07**

vector, but only with the proportion of each element. Table III indicates the cosine angle between the decomposition vector of quad-polarimetric and HCP in five ROIs under GF-3 data .The bold entities indicates the minimum value of each line. Cosine angles of the proposed GTM method in the five regions are $6.41°, 12.49°, 6.14°, 5.05°$, and $0.24°$, respectively. The cosine angles of GTM method are the smallest except for the forest area. The high cosine angle of the forest area is because the volume scattering component in G4U is only 72.95%, whereas the volume scattering component obtained by GTM is relatively higher in several HCP decomposition methods. However, although the cosine angle of GTM in forest area is higher, it is only $0.72°$ higher than the lowest HTM. In particular, the cosine angle of Wang's methods is $18.24°$ in forest area, which is much higher than other decomposition methods. This is due to its severe underestimation of the volume scattering component in this area. The average results demonstrate that GTM method has the smallest cosine angle with the quad-polarimetric decomposition vector, which is only $6.07°$. This also proves that GTM has the closest decomposition result to G4U and can be used as an approximation to the quad-polarimetric decomposition method.

In order to verify the universality of the proposed method, the RADARSAT-2 quad-polarimetric image (acquired on March 7, 2019) of the same region is selected for further analysis.

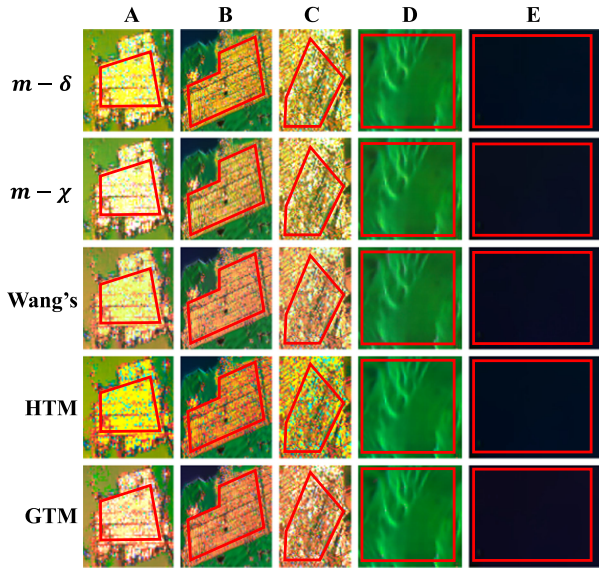

Fig. 7. Enlarged view of Patch A (Orthogonal Urban), Patch B (Oriented Urban 1), Patch C (Oriented Urban 2), Patch D (Forest), and Patch E (Water) in Fig. 6.

The pixel distance of RADARSAT-2 is 4.7 m in both range and azimuth directions. The window size was set as 5×5, corresponding to 22 m by 22 m on the ground area. Fig. 6 shows the pseudocolor-coded images of five decomposition methods. Five ROIs similar to the GF-3 data were also selected labeled by the red-colored boxes for statistics analysis. The corresponding relationship is the same as GF-3, namely A (Orthogonal Urban Area), B (Oriented Urban Area 1), C (Oriented Urban Area 2), D (Forest Area), and E (Water Area), respectively. The enlarge view of the five ROIs is given in Fig. 7 and detailed statistical information in Table IV.

TABLE IV
STATISTICS OF RADARSAT-2 IMAGE DECOMPOSITION RESULTS

	Orthogonal Urban			Oriented Urban 1			Oriented Urban 2			Forest			Water		
	P_d	P_v	P_s	P_d	P_v	P_s	P_d	P_v	P_s	P_d	P_v	P_s	P_d	P_v	P_s
$m-\delta$	60.55	29.85	9.61	52.19	39.58	8.23	42.42	27.53	30.05	0.28	89.62	10.09	0.67	22.12	77.21
$m-\chi$	52.86	29.85	17.30	47.62	39.58	12.80	41.69	27.53	30.78	0.51	89.62	9.87	3.25	22.12	74.64
Wang's	67.22	19.40	13.38	62.10	25.73	12.18	59.42	17.89	22.69	16.00	58.25	25.75	4.61	14.38	81.01
HTM	66.81	25.33	7.85	60.27	34.87	4.86	56.34	25.25	18.41	0.00	89.62	10.38	0.64	20.24	79.12
GTM	68.12	17.63	14.25	62.51	24.78	12.70	59.43	17.78	22.80	0.14	90.30	9.57	4.64	14.22	81.13

Note: Scattering mechanisms contribution (%) of different decomposition methods in five ROIs.

It is worth noting that although the five ROIs are similar to the GF-3 dataset, the system parameters, imaging trajectory, and incident angle of the two SAR sensors are slightly different. Since the polarization characteristics are very sensitive to these factors, there are some differences in the decomposition results. From Fig. 6, several decomposition methods can accurately identify the dominant scattering mechanism, but there are differences in specific contributions. For urban areas (Patches A, B, and C), as the orientation angle of the urban increases, the contribution of dihedral angle scattering obtained by all methods decreases. However, the model-based decomposition method can always obtain a higher dihedral scattering contribution estimate than the WDT-based method, and the contribution P_d obtained by the three model-based methods are similar. Besides, GTM and Wang's methods can effectively reduce the volume scattering estimation in urban areas when compared with the HTM method.

No surprising, Wang's method also incorrectly estimated the volume scattering component of the forest area. However, the proposed GTM method can still get the highest estimated value of volume scattering component, which is 0.68% higher than $m-\delta$, $m-\chi$, and HTM methods. In the water area, the proportions of the surface scattering components obtained by the five decomposition methods are 77.21%, 74.64%, 81.01%, 79.12%, and 81.13%, respectively. The model-based decomposition methods can obtain relatively high surface scattering components. Similarly, Wang's and GTM have better performance than HTM in volume scattering estimation.

We also evaluated the similarity between the results of different HCP decomposition method and the quad-polarimetric G4U method on the RADARSAT-2 dataset. The average cosine angle is directly given here, which are $10.26^\circ, 10.44^\circ, 7.12^\circ, 9.26^\circ$, and 6.56° for $m-\delta$, $m-\chi$, Wang's, HTM, and GTM method, respectively. It can conclude that the GTM method can still achieve the closest result to quad-polarimetric decomposition method, which also shows the effectiveness of the proposed method.

V. DISCUSSION

A. Theoretical Performance

In general, the model-based method has better performance than the WDT-based method in the area dominated by surface and dihedral scattering mechanism. Among model-based methods, Wang's method is not suitable for volume scattering dominant area and the proposed GTM method performs best in various scenarios. This section will theoretically analyze the reasons for these results.

TABLE V
THEORETICAL PERFORMANCE ANALYSIS OF DIFFERENT DECOMPOSITION METHODS

	$m-\delta$	$m-\chi$	Wang's	HTM	GTM
Ideal Surface Model	✓	✓	✓	✓	✓
Bragg Surface Model			✓	✓	✓
Ideal Dihedral Model	✓	✓	✓	✓	✓
Fresnel Dihedral Model			✓	✓	✓
Freeman Volume Model	✓	✓		✓	✓
Yamaguchi Volume Model				✓	✓
Arii Volume Model					✓

Note: Symbol "✓" indicates the method can well identify the corresponding pure scattering mechanism.

Seven models of three pure scattering mechanisms (in Stokes form) are chosen to analyze the performance of different HCP decomposition methods, which includes pure surface scattering mechanism (ideal and Bragg surface scattering model), pure dihedral scattering mechanism (ideal and Fresnel surface scattering model), and pure volume scattering mechanism (Freeman, Yamaguchi, and Arii). Theoretically, an effective decomposition method should be able to identify these special pure scattering mechanisms accurately. For example, for the pure surface scattering mechanism, the dihedral and volume scattering power in the decomposition results should be 0.

The Stokes vector of the pure surface scattering mechanism is shown in (7), and its DoP is 1. Therefore, the volume scattering power obtained by the WDT-based method is 0 according to (3). When further distinguishing the surface and dihedral scattering power, both χ and θ are related to $|\beta|$. Only when $|\beta| = 0$, then $\sin\delta = 1$ and $\sin 2\chi = 1$, the dihedral scattering power is 0, and the model degenerates to an ideal surface scattering model. This indicates that the WDT-based methods can well identify the ideal surface scattering mechanism but cannot identify the Bragg scattering mechanism. This derivation process is consistent with pure dihedral scattering model, and the corresponding conclusions are also shown in Table V. Among them, the symbol "✓" indicates the method can well identify the pure scattering mechanism.

As mentioned in Section III, the Freeman volume scattering model is consistent with the form of the CD wave. Since its DoP is 0, $P_v = g_0$ is obtained through (3). This means that the WDT-based decomposition methods can accurately identify the

Freeman volume scattering model. However, WDT-based decomposition methods cannot accurately identify the Yamaguchi and Arii volume scattering models since the DoP is not 0. The proposed GTM method can well identify these pure scattering mechanisms according to Section III. For Wang's and HTM methods, the decomposition results of the seven scattering models can also be obtained step by step, which will not be further expanded here and the corresponding results are presented in Table V.

From Table V, the WDT-based decomposition methods can only accurately identify two ideal scattering mechanisms and Freeman volume scattering model, whereas model-based decomposition methods can further accurately identify the pure scattering mechanism in the form of Bragg and Fresnel model. This reflects the superiority of the model-based method and explains the good performance of it in urban and water area. In the model-based decomposition methods, Wang's method works well when dealing with pure surface scattering and dihedral scattering mechanisms, but cannot even accurately identify the Freeman volume scattering model. This is due to the scale factor in volume scattering component estimation, which is corresponded with its terrible performance in forest area. HTM method can well identify all the pure scattering mechanisms except Arii volume scattering model. It is easy to understand as only Freeman and Yamaguchi volume scattering models are considered in the model establishment. It worth noticing that the proposed GTM method can accurately identify all the special forms of pure scattering mechanisms, which demonstrates the universality of GTM. Combining results in Section IV and Table V, it is obvious that methods performing well on pure scattering mechanisms can also achieve better performance in real data.

B. Roll-Invariant Characteristics

In quad-polarimetric decomposition, it is often necessary to perform polarimetric orientation compensation to obtain better performance. Correspondingly, the form of the Stokes vector after orientation compensation is [31]

$$\mathbf{G}(\varphi) = \begin{bmatrix} g_0 \\ g_1 \cos 2\varphi + g_2 \sin 2\varphi \\ -g_1 \sin 2\varphi + g_2 \cos 2\varphi \\ g_3 \end{bmatrix} \tag{30}$$

where φ is the polarimetric orientation angle that can be calculated through digital elevation model or estimated from quad-polarimetric data. However, there is currently no suitable method to obtain an accurate estimate for compact polarimetry. Therefore, an effective method is to develop a decomposition method that is not sensitive to the orientation angle. In other words, the decomposition result is required to have rotation invariance.

It can be concluded from (30) that g_0, g_3, and $\sqrt{g_1^2 + g_2^2}$ are roll-invariant variables. Thus, if only these three variables are used in the decomposition process, the corresponding decomposition method is roll-invariant. It is obvious that WDT-based decomposition methods are roll-invariant. For the model-based decomposition method, the key lies in the volume scattering model. Wang's method and the proposed method satisfy the roll-invariant characteristics.

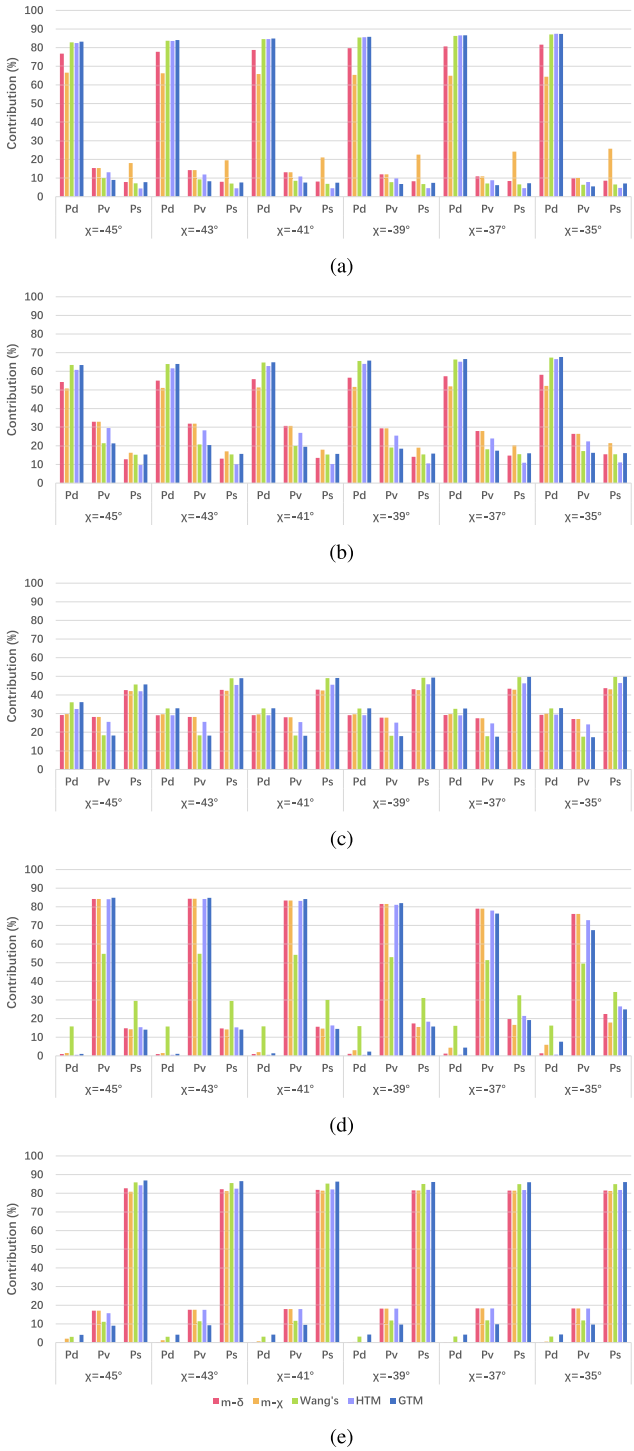

Fig. 8. Decomposition results under different emission ellipticities of GF-3 dataset. The five colors in the figure represent five different decomposition methods. From top to bottom are (a) Orthogonal Urban, (b) Oriented Urban 1, (c) Oriented Urban 2, (d) Forest, and (e) Water.

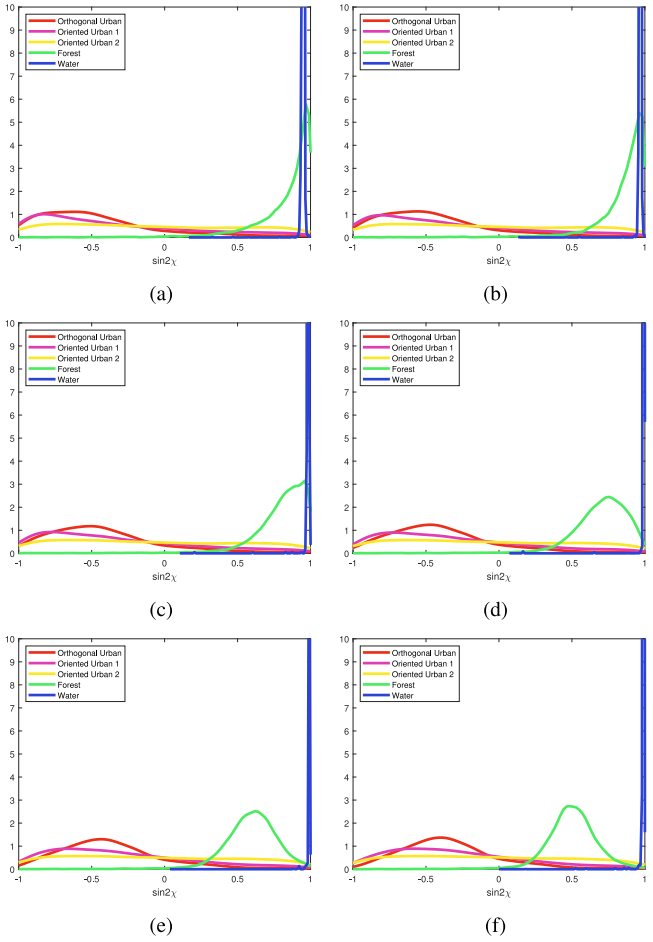

Fig. 9. PDF of $\sin 2\chi$ under different emission ellipticities of GF-3 dataset. (a) $\chi = -45°$. (b) $\chi = -43°$. (c) $\chi = -41°$. (d) $\chi = -39°$. (e) $\chi = -37°$. (f) $\chi = -35°$.

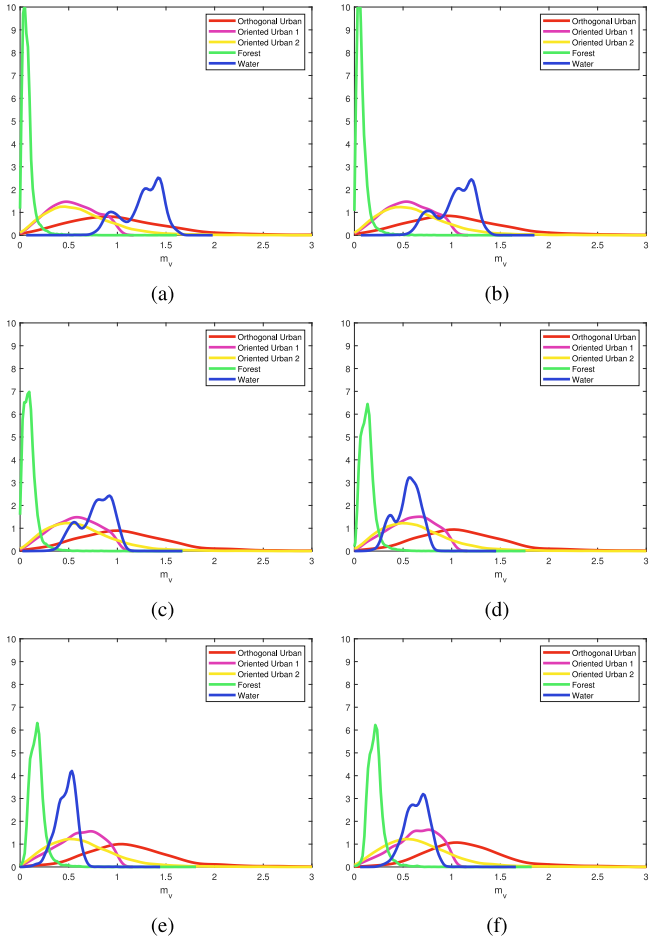

Fig. 10. PDF of m_v under different emission ellipticities of GF-3 dataset. (a) $\chi = -45°$. (b) $\chi = -43°$. (c) $\chi = -41°$. (d) $\chi = -39°$. (e) $\chi = -37°$. (f) $\chi = -35°$.

C. *Effect of Transmission Distortion*

In actual SAR systems, the emitted electromagnetic waves are often not ideal circularly polarized waves [32]. Therefore, the influence of ellipticity distortion on the decomposition results is analyzed. With reference to the analysis of Kumar *et al.* [14], here we use GF-3 data to analyze the influence when the emission ellipticities are at $-45°$, $-43°$, $-41°$, $-39°$, $-37°$, and $-35°$. The decomposition results under different ellipticities are given in Fig. 8. The distribution of the five subfigure from top to bottom corresponds to the results of five different ROIs, orthogonal Urban, Oriented Urban 1, Oriented Urban 2, Forest, and Water areas. The five colors in the figure represent the five different decomposition methods mentioned earlier.

The following conclusions can be drawn from Fig. 8. As the emission error increases (ellipticity changes from $-45°$ to $-35°$), the decomposition results show a certain difference. The water area is least affected by the emission distortion among all the ROIs, and the overall change of each component does not exceed 2%. For Orthogonal Urban and Oriented Urban 1, the contribution of the dihedral scattering component increases slightly with the increase of emission distortion, whereas for Oriented Urban 2, the contribution of the surface scattering component increases slightly with the increase of emission distortion. In fact, the decomposition results are not significantly affected by the emitted distortion except for the forest area, and the volume scattering contribution of all decomposition methods is greatly reduced as the emission distortion increases in forest area. The deviation of the volume scattering component contribution obtained by the five methods at $-35°$ (equivalent to 3 dB of emission axis ratio) is 8.03%, 5.22%, 11.24%, and 17.38%, respectively. The results demonstrate that the proposed method is more sensitive to emission distortion in forest area. In order to further explore the reasons for this phenomenon, we analyze the influence of emission distortion on the stage of dominant scattering mechanism determination.

Figs. 9 and 10, respectively, show the pdfs of $\sin 2\chi$ and m_v under different emission ellipticities. From Fig. 9, signs of $\sin 2\chi$ in water and three urban areas hardly change with the emission distortion. For the forest area, $\sin 2\chi$ increases with the increase of the transmission distortion, but the g_3 element in forest area is still positive when emission ellipticity reaches $-35°$. The aforementioned analysis suggests that the emission distortion has little effect on distinguishing the surface and the dihedral

scattering dominant area. Next, we will analyze the influence of emission distortion on distinguishing the dominant area of volume scattering.

Fig. 10 shows that as the emission distortion increases, m_v in forest area and water area is increasing and decreasing, respectively, whereas it in the urban area changes little. Due to these changing characteristics, the threshold $m\text{th} = 0.2$ that can distinguish the forest area in Fig. 10(a) is no longer working well in Fig. 10(f). This is also the reason why the estimated volume scattering component obtained by the proposed method in the forest area changes greatly when the emission error is large. A large number of pixels that should have been judged to be dominated by volume scattering are misjudged now.

Combining Figs. 9 and 10, we can conclude that the characteristic parameters of the forest area are more sensitive to emission distortion than other areas. Thus, special attention should be paid to the nature of the forest area when the emission distortion is large. Furthermore, Fig. 10(c) and (d) indicates that the segmentation threshold proposed in this article is roughly effective when the emission ellipticity angle is -45° to -40°, and the emission axis ratio range is less than 1.5 dB. Therefore, in the case that the known emission axis ratio is greater than 1.5 dB, the criterion of the dominant volume scattering mechanism should be reconsidered. The appropriate discrimination threshold can be reselected or other methods can be used.

VI. Conclusion

There are currently two types of HCP decomposition methods, WDT-based and model-based decomposition methods. Considering the robust physical meaning of the model-based method, this article proposed a GTM. By introducing Arii general volume scattering model, GTM improves the ability to recognize complex volume scattering mechanisms. In addition, GTM is solved separately when the three scattering mechanisms are dominant. In each case, the scattering component model that contributes less can be simplified. This not only ensures the universality of the decomposition method but also facilitates the solution process for HCP data.

Theoretical analysis has proved that GTM method can identify various different pure scattering mechanisms. Also, experiments based on the emulated data show that the model-based methods perform better in the area dominated by surface and dihedral scattering mechanism and the proposed GTM method further improves the performance of the model-based decomposition method in the area dominated by volume scattering mechanism. The similarity between HCP and quad-polarimetric decomposition results based on the cosine angle is compared for the first time and the results demonstrate that the proposed method can achieve the closest results to quad-polarimetric. In addition, precautions for circularly polarized wave emission distortion are also discussed in this article.

References

[1] R. K. Raney, "Hybrid dual-polarization synthetic aperture radar," *Remote Sens.*, vol. 11, no. 13, 2019, Art. no. 1521.

[2] M. Mahdianpari *et al.*, "Mid-season crop classification using dual-, compact-, and full-polarization in preparation for the RADARSAT constellation mission (RCM)," *Remote Sens.*, vol. 11, no. 13, 2019, Art. no. 1582.

[3] F. Xu, Q. Song, and Y. Jin, "Polarimetric SAR image factorization," *IEEE Trans. Geosci. Remote Sens.*, vol. 55, no. 9, pp. 5026–5041, Sep. 2017.

[4] D. Ratha, E. Pottier, A. Bhattacharya, and A. C. Frery, "A PolSAR scattering power factorization framework and novel roll-invariant parameter-based unsupervised classification scheme using a geodesic distance," *IEEE Trans. Geosci. Remote Sens.*, vol. 58, no. 5, pp. 3509–3525, May 2020.

[5] S. Dey, A. Bhattacharya, D. Ratha, D. Mandal, and A. C. Frery, "Target characterization and scattering power decomposition for full and compact polarimetric SAR data," *IEEE Trans. Geosci. Remote Sens.*, vol. 59, no. 5, pp. 3981–3998, 2021, doi={10.1109/TGRS.2020.3010840.

[6] F. Xu, Y. Li, and Y. Jin, "Polarimetric-anisotropic decomposition and anisotropic entropies of high-resolution SAR images," *IEEE Trans. Geosci. Remote Sens.*, vol. 54, no. 9, pp. 5467–5482, Sep. 2016.

[7] Jong-Sen Lee and E. Pottier, *Polarimetric Radar Imaging: From Basics to Applications*. Boca Raton, FL, USA: CRC Press, 2017.

[8] A. Kumar, R. K. Panigrahi, and A. Das, "Three-component decomposition technique for hybrid-pol SAR data," *IET Radar, Sonar Navigat.*, vol. 10, no. 9, pp. 1569–1574, 2016.

[9] R. K. Raney, "Hybrid-polarity SAR architecture," *IEEE Trans. Geosci. Remote Sens.*, vol. 45, no. 11, pp. 3397–3404, Nov. 2007.

[10] F. J. Charbonneau *et al.*, "Compact polarimetry overview and applications assessment," *Can. J. Remote Sens.*, vol. 36, no. sup2, pp. S298–S315, 2010.

[11] S. R. Cloude, D. G. Goodenough, and H. Chen, "Compact decomposition theory," *IEEE Geosci. Remote Sens. Lett.*, vol. 9, no. 1, pp. 28–32, Jan. 2012.

[12] R. K. Raney, J. T. S. Cahill, G. W. Patterson, and D. B. J. Bussey, "The m-chi decomposition of hybrid dual-polarimetric radar data with application to lunar craters," *J. Geophys. Res.*, vol. 117, no. E12, 2012.

[13] M. Ghanbari, D. A. Clausi, L. Xu, and M. Jiang, "Contextual classification of sea-ice types using compact polarimetric SAR data," *IEEE Trans. Geosci. Remote Sens.*, vol. 57, no. 10, pp. 7476–7491, Oct. 2019.

[14] V. Kumar, H. McNairn, A. Bhattacharya, and Y. S. Rao, "Temporal response of scattering from crops for transmitted ellipticity variation in simulated compact-pol SAR data," *IEEE J. Sel. Topics Appl. Earth Observ. Remote Sens.*, vol. 10, no. 12, pp. 5163–5174, Dec. 2017.

[15] A. Bhattacharya, S. De, A. Muhuri, M. Surendar, G. Venkataraman, and A. K. Das, "A new compact polarimetric SAR decomposition technique," *Remote Sens. Lett.*, vol. 6, no. 12, pp. 914–923, 2015.

[16] V. Kumar, D. Mandal, A. Bhattacharya, and Y. S. Rao, "Crop characterization using an improved scattering power decomposition technique for compact polarimetric SAR data," *Int. J. Appl. Earth Observ. Geoinf.*, vol. 88, 2020, Art. no. 102052.

[17] A. Freeman and S. L. Durden, "A three-component scattering model for polarimetric SAR data," *IEEE Trans. Geosci. Remote Sens.*, vol. 36, no. 3, pp. 963–973, May 1998.

[18] Y. Yamaguchi, T. Moriyama, M. Ishido, and H. Yamada, "Four-component scattering model for polarimetric SAR image decomposition," *IEEE Trans. Geosci. Remote Sens.*, vol. 43, no. 8, pp. 1699–1706, Aug. 2005.

[19] R. Guo, W. He, S. Zhang, B. Zang, and M. Xing, "Analysis of three-component decomposition to compact polarimetric synthetic aperture radar," *IET Radar, Sonar Navigat.*, vol. 8, no. 6, pp. 685–691, 2014.

[20] H. Wang, Z. Zhou, J. Turnbull, Q. Song, and Q. Feng, "Three-component decomposition based on stokes vector for compact polarimetric SAR under the CTLR mode," in *Proc. Eur. Radar Conf.*, 2015, pp. 73–76.

[21] M. Arii, J. J. van Zyl, and Y. Kim, "A general characterization for polarimetric scattering from vegetation canopies," *IEEE Trans. Geosci. Remote Sens.*, vol. 48, no. 9, pp. 3349–3357, Sep. 2010.

[22] M. Arii, J. J. van Zyl, and Y. Kim, "Adaptive model-based decomposition of polarimetric SAR covariance matrices," *IEEE Trans. Geosci. Remote Sens.*, vol. 49, no. 3, pp. 1104–1113, Mar. 2011.

[23] A. Kumar, A. Das, and R. K. Panigrahi, "Hybrid-pol based three-component scattering model for analysis of RISAT data," *IEEE J. Sel. Topics Appl. Earth Observ. Remote Sens.*, vol. 10, no. 12, pp. 5155–5162, Dec. 2017.

[24] A. Freeman, "Fitting a two-component scattering model to polarimetric SAR data from forests," *IEEE Trans. Geosci. Remote Sens.*, vol. 45, no. 8, pp. 2583–2592, Aug. 2007.

[25] W. An, Y. Cui, and J. Yang, "Three-component model-based decomposition for polarimetric SAR data," *IEEE Trans. Geosci. Remote Sens.*, vol. 48, no. 6, pp. 2732–2739, Jun. 2010.

[26] O. Antropov, Y. Rauste, and T. Hame, "Volume scattering modeling in PolSAR decompositions: Study of ALOS PALSAR data over boreal

forest," *IEEE Trans. Geosci. Remote Sens.*, vol. 49, no. 10, pp. 3838–3848, Oct. 2011.
[27] M. Neumann, L. Ferro-Famil, and A. Reigber, "Estimation of forest structure, ground, and canopy layer characteristics from multibaseline polarimetric interferometric SAR data," *IEEE Trans. Geosci. Remote Sens.*, vol. 48, no. 3, pp. 1086–1104, Mar. 2010.
[28] J. Chen, Y. Chen, W. An, Y. Cui, and J. Yang, "Nonlocal filtering for polarimetric SAR data: A pretest approach," *IEEE Trans. Geosci. Remote Sens.*, vol. 49, no. 5, pp. 1744–1754, May 2011.
[29] J. T. Pulliainen, K. Heiska, J. Hyyppa, and M. T. Hallikainen, "Backscattering properties of boreal forests at the C- and X-bands," *IEEE Trans. Geosci. Remote Sens.*, vol. 32, no. 5, pp. 1041–1050, Sep. 1994.
[30] G. Singh, Y. Yamaguchi, and S. Park, "General four-component scattering power decomposition with unitary transformation of coherency matrix," *IEEE Trans. Geosci. Remote Sens.*, vol. 51, no. 5, pp. 3014–3022, May 2013.
[31] J. Yin, J. Yang, Z. Zhou, and J. Song, "The extended Bragg scattering model-based method for ship and oil-spill observation using compact polarimetric SAR," *IEEE J. Sel. Topics Appl. Earth Observ. Remote Sens.*, vol. 8, no. 8, pp. 3760–3772, Aug. 2015.
[32] R. Touzi, M. Shimada, T. Motohka, and S. Nedelcu, "Assessment of PALSAR-2 compact non-circularity using Amazonian rainforests," *IEEE Trans. Geosci. Remote Sens.*, vol. 58, no. 10, pp. 7472–7482, Oct. 2020.

Wentao Hou received the B.S. degree in Communication engineering from Xidian University, Xi'an, China, in 2017. He is currently working toward the Ph.D. degree in Communication and information systems with the Department of Space Microwave Remote Sensing System, Aerospace Information Research Institute, Chinese Academy of Sciences, Beijing, China.

He is currently with the University of Chinese Academy of Sciences, Beijing, China. His research interests include polarimetric/compact polarimetric SAR image processing, and information extraction.

Fengjun Zhao received the M.S. and Ph.D. degrees in engineering from the Institute of Electronics, Chinese Academy of Sciences (IECAS), Beijing, China, in 1995 and 2012, respectively.

In 1995, he joined the Department of Space Microwave Remote Sensing System, IECAS, where he worked on spaceborne/airborne SAR system design. He has been the Leader of some spaceborne/airborne SAR programs. He is currently the Director with the Department of Aerospace Products Production, Aerospace Information Research Institute, Chinese Academy of Sciences. His research interests include spaceborne/airborne SAR system design, ground moving target identification, multichannel SAR signal processing, and circuit design.

Dr. Zhao was the recipient of the First Prize of the National Science And Technology Progress, the First Prize of National Defense Science and Technology Progress, and the Outstanding Achievement Award of Chinese Academy of Sciences.

Xiuqing Liu received the Ph.D. degree in engineering from the Graduate University of Chinese Academy of Sciences, Beijing, China, in 2004.

She is currently an Associate Researcher with the Aerospace Information Research Institute, Chinese Academy of Sciences. Her main research interests include polarimetric/compact polarimetric SAR system technology, polarimetric/compact polarimetric SAR data processing, and information extraction.

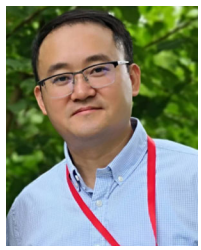

Robert Wang (Senior Member, IEEE) received the B.S. degree in control engineering from Henan University, Kaifeng, China, in 2002, and the Dr.Eng. degree from the Graduate University of Chinese Academy of Sciences, Beijing, China, in 2007 .

In 2007, he joined the Center for Sensor Systems (ZESS), University of Siegen, Siegen, Germany. He was involved in various joint projects supported by ZESS and Fraunhofer-FHR, Wachtberg, Germany, e.g., the TerraSAR-X/phased array multifunctional imaging radar (PAMIR) hybrid bistatic synthetic aperture radar (SAR) experiment, the PAMIR/stationary bistatic SAR experiment, the PAMIR/stationary bistatic SAR experiment with nonsynchronized oscillator, and the millimeter-wave frequency-modulated continuous wave SAR data processing. Since 2011, he has been a Research Fellow with the Department of Spaceborne Microwave Remote Sensing System, Institute of Electronics, Chinese Academy of Sciences, Beijing, China, where he was funded by the Hundred Talents Program of the Chinese Academy of Sciences. Since 2012, he has been a Co-Principal Investigator (PI) with the Helmholtz-CAS Joint Research Group, Beijing, China, concerning spaceborne microwave remote sensing for prevention and forensic analysis of natural hazards and extreme events. He is also responsible for several national high-resolution spaceborne imaging radar missions supported by the National High-Resolution Earth Observation Major Special Program. He is also the PI of two advanced L-band spaceborne SAR systems that are aimed at global dynamic earth monitoring. He has authored or coauthored more than 100 peer-reviewed journal articles in the field of SAR imaging technology and authored *Bistatic SAR System and Signal Processing Technology* (Springer, 2017). His research interests include monostatic and multistatic SAR imaging and high-resolution wide-swath spaceborne SAR system and imaging models.

Dr. Wang was the recipient of the National Ten Thousand Talent Program-Young Top-Notch Talent Program Award in 2014, the National Natural Science Funds of China for Excellent Young Scholar in 2014, the Zhao Jiuzhang Award for Outstanding Young Science in 2015, the First Prize for Military Scientific and Technological Progress in 2016, the Scientific and Technological Innovation Leading Talent by National High-Level Talents Special Support Plan in 2017, and the Distinguished Young Scholars from the National Natural Science Foundation of China in 2018. He was the Session Chair at the European Conference on Synthetic Aperture Radar (EUSAR) and the International Geoscience and Remote Sensing Symposium (IGARSS) from 2012 to 2016. He has contributed to invited sessions at the EUSAR from 2008 to 2016, the European Radar Conference in 2009, and IGARSS from 2012 to 2016. Since 2020, he has been an Associate Editor for the IEEE TRANSACTIONS ON GEOSCIENCE AND REMOTE SENSING.